DispatchDate: 07.05.2022 · ProofNo: 797, p.1

nature catalysis

ARTICLES

https://doi.org/10.1038/s41929-022-00797-0

Experimental Sabatier plot for predictive design of active and stable Pt-alloy oxygen reduction reaction catalysts

Jin Huang[1], Luca Sementa[2], Zeyan Liu[1], Giovanni Barcaro[2], Miao Feng[1,3], Ershuai Liu[4], Li Jiao[4], Mingjie Xu[5,6], Denis Leshchev[7], Sung-Joon Lee[1], Mufan Li[8], Chengzhang Wan[8], Enbo Zhu[1], Yang Liu[1], Bosi Peng[8], Xiangfeng Duan[8,9], William A. Goddard III[10] ✉, Alessandro Fortunelli[2] ✉, Qingying Jia[4] ✉ and Yu Huang[1,9] ✉

A critical technological roadblock to the widespread adoption of proton-exchange membrane fuel cells is the development of highly active and durable platinum-based catalysts for accelerating the sluggish oxygen reduction reaction, which has largely relied on anecdotal discoveries to date. While the oxygen binding energy ΔE_O has been frequently used as a theoretical descriptor for predicting the activity, there is no known descriptor for the durability prediction. Herein, we developed a binary experimental descriptor that captures both the strain and Pt transition metal coupling contributions through X-ray absorption spectroscopy, and directly correlated the binary experimental descriptor with the calculated ΔE_O of the catalyst surface. This leads to an experimentally validated Sabatier plot to predict both the catalytic activity and stability for a wide range of platinum-alloy oxygen reduction reaction catalysts. Based on the binary experimental descriptor, we further designed an oxygen reduction reaction catalyst wherein high activity and stability are simultaneously achieved.

Platinum alloys are the most frequently adopted electrocatalysts for accelerating the sluggish oxygen reduction reaction (ORR) at the cathode of proton-exchange membrane fuel cells (PEMFCs)[1,2]. However, the high cost of Pt limits the practical widespread adoption of PEMFCs[3–5]. This has motivated intensive studies on Pt-based ORR catalysts, aiming to provide a major leap in activity and stability with reduced usage of Pt. The ORR activity is believed to scale with the core-level binding energy of oxygen to the catalyst, ΔE_O, as proposed by Nørskov et al.[2], which can be predicted through quantum mechanics calculations. General analysis based on the Sabatier principle indicates that a catalyst surface that binds oxygen about 0.2 eV more weakly than Pt(111) does yields the best intrinsic activity[2,6,7]. A generally effective approach to improve ORR activity is through alloying Pt with transition metals, M (M = Pd, Fe, Co, Ni and so on)[8–10], which introduces the strain effect and/or ligand effect that modulate the ΔE_O. It has been proposed that the strain effect leads to a downshift of the Pt *d*-band centre relative to the Fermi level, while the ligand effect modifies the electronic structure of the near-surface Pt, both of which can weaken the ΔE_O to improve the ORR activity[11–14].

While the quantum-mechanics-derived ΔE_O has been widely acknowledged as a useful descriptor, its experimental analogue has met very limited success, which severely limits the efficient development of high-performing Pt-based nanocatalysts. For example, strain in Pt alloys has been routinely adopted as a plausible experimental descriptor for ORR activity[14–16]. However, strain alone is insufficient to predict the ORR activity of Pt-alloy nanocatalysts[17,18]. Meanwhile, the ligand effect[19] and local atomic coordination[20], which describe the contributions from both composition and atomic coordination distribution to ΔE_O, and hence to the catalytic activities of Pt alloys, have rarely been investigated or accounted for experimentally because of their poor attainability in experiments. Moreover, the ever-evolving structure and composition of catalysts during catalysis[21,22] adds to the challenge of identifying simple experimentally tangible descriptors that can capture the key contributing factors predicted in theory[19,23,24]. These persisting issues have plagued the development of high-performing ORR catalysts and show the need for an experimental, tangible descriptor to predict both the activity and stability of these catalysts.

To date, the developments of highly active and stable Pt-alloy nanocatalysts have largely relied on anecdotal discoveries[25–27]. Herein, by combining theoretical modelling and experimental observations, we developed a binary experimental descriptor (BED) based on the average Pt–Pt bond length from extended X-ray absorption fine structure (EXAFS; strain; Supplementary Note 1) and the asymmetry factor (AF; Supplementary Note 2 and Supplementary Fig. 1) in the Pt L_3 X-ray absorption near edge structure (XANES) spectra of Pt alloys. We showed that the BED can be used to accurately reflect the calculated oxygen binding energy ΔE_O of the Pt-alloy catalyst surface (Supplementary Note 3), leading to

[1]Department of Materials Science and Engineering, University of California, Los Angeles, CA, USA. [2]CNR-ICCOM & IPCF, Consiglio Nazionale delle Ricerche, Pisa, Italy. [3]College of Materials Science and Engineering, Fuzhou University, Fuzhou, P. R. China. [4]Department of Chemistry and Chemical Biology, Northeastern University, Boston, MA, USA. [5]Irvine Materials Research Institute, University of California, Irvine, CA, USA. [6]Department of Materials Science, University of California, Irvine, CA, USA. [7]National Synchrotron Light Source II, Brookhaven National Laboratory, Upton, NY, USA. [8]Department of Chemistry and Biochemistry, University of California, Los Angeles, CA, USA. [9]California NanoSystems Institute, University of California, Los Angeles, CA, USA. [10]Materials and Process Simulation Center, California Institute of Technology, Pasadena, CA, USA. ✉e-mail: wag@wag.caltech.edu; alessandro.fortunelli@cnr.it; qjia@iit.edu; yhuang@seas.ucla.edu

the establishment of an experimental Sabatier plot that can be used to comprehensively predict the activity and stability of Pt-alloy ORR catalysts. Furthermore, based on the established Sabatier plot, we demonstrated the design of a PtNiCo catalyst that simultaneously delivers a superior specific activity (SA) of $10.7 \pm 1.4\,mA\,cm^{-2}$, a mass activity (MA) of $7.1 \pm 1.0\,A\,mg_{Pt}^{-1}$ at 0.9 V versus the reversible hydrogen electrode (RHE) and an exceptionally high stability showing only 8% loss of electrochemically active surface area (ECSA) and 12% loss of MA after 20,000 cycles of accelerated degradation tests (ADT), filling in the blank in the design space for ORR catalysts.

Results

Design and comparison of slow- and fast-dealloyed PtNi catalysts. To deconvolute and understand the key experimental signatures leading to the different activities and stabilities of Pt-alloy catalysts, we compare catalysts with similar morphologies and compositions to discern the nuanced performances. We hence chose the concave octahedral PtNi catalysts with a commonly observed stable final composition of ~80 at.% Pt and with a Pt-rich surface under electrochemical conditions[21,28,29]. We designed and compared the performance between the fast-dealloyed PtNi (fd-PtNi) octahedral catalysts obtained through aggressive acid dealloying of the PtNi octahedral catalysts, and the slow-dealloyed PtNi (sd-PtNi) octahedral catalysts obtained through gradual dealloying in air-purged *N*,*N*-dimethylformamide (DMF). Both catalysts showed a similar concave octahedral morphology with similar composition after the electrochemical activation process (Fig. 1a–h). To prepare the concave PtNi catalysts, the transition-metal-rich octahedral parent $Pt_{45}Ni_{55}$/C (p-$Pt_{45}Ni_{55}$) was first synthesized using a modified one-pot synthesis method reported previously[30] (Methods). The transmission electron microscopy (TEM) and high-angle annular dark-field scanning TEM (HAADF-STEM) images (Fig. 1c) of the p-$Pt_{45}Ni_{55}$ showed an octahedral shape with an average edge length of 7.0 ± 0.8 nm (Supplementary Fig. 2a) and an average lattice spacing of 0.212 nm according to the fast Fourier transform diffraction pattern (inset of Fig. 1c) and X-ray diffraction results (Supplementary Fig. 3a). The p-$Pt_{45}Ni_{55}$ was then subject to either a slow-dealloying or a fast-dealloying process to obtain the sd-PtNi or the fd-PtNi catalysts, respectively. Both sd-PtNi and fd-PtNi showed a highly concave morphology (Fig. 1b,d) with a composition around $Pt_{85}Ni_{15}$ (Supplementary Figs. 3 and 4b).

To obtain sd-PtNi, the p-$Pt_{45}Ni_{55}$ catalysts were dispersed in DMF solution and heated to 120 °C under an air purge to allow slow dissolution of Ni (Methods). This slow process allowed additional time for the remaining atoms to rearrange themselves into a structure closer to equilibrium[31], achieving stable, concave sd-PtNi catalysts. The changes in the structure and composition of octahedral sd-PtNi catalysts were traced by X-ray diffraction over the course of the slow dealloying (Supplementary Fig. 3a). It was observed that the main X-ray diffraction peaks shifted continuously towards low angles, indicating the lattice spacing relaxation due to transformation from Ni-rich alloys to Pt-rich alloys, and stabilized after three days of dealloying (Supplementary Fig. 3a). The average (111) lattice spacing in the sd-PtNi shifted to 0.223 nm from 0.212 nm (Supplementary Fig. 3c), indicating a composition change from $Pt_{45}Ni_{55}$ to $Pt_{75}Ni_{25}$ based on Vegard's law, which is consistent with the energy-dispersive X-ray (EDX) results ($Pt_{45}Ni_{55}$ to $Pt_{76}Ni_{24}$; Supplementary Fig. 3a). TEM studies also revealed that the octahedra evolved to the concave octahedra after three days of dealloying (Supplementary Figs. 2c and 3b). The resulting sd-$Pt_{76}Ni_{24}$ further evolved to highly concave sd-$Pt_{85}Ni_{15}$ after electrochemical activation, according to the EDX spectroscopy results (Fig. 1d and Supplementary Fig. 3f). The EDX mapping and line-scan profile of sd-$Pt_{85}Ni_{15}$ showed a Pt skin of about 0.7 nm after the activation process (Fig. 1g). The fd-$Pt_{86}Ni_{14}$ catalysts were obtained through a fast 0.5 M sulfuric acid leaching treatment of the p-$Pt_{45}Ni_{55}$ (Methods). The resulting fd-$Pt_{86}Ni_{14}$ showed a similar highly concave morphology and similar composition to the sd-$Pt_{85}Ni_{15}$ (Supplementary Fig. 3g), together with a similar Pt-skin structure after electrochemical activation (Fig. 1b,e and Supplementary Fig. 4c,d). In addition, the ECSA was determined to be $65\,m^2\,g_{Pt}^{-1}$ for sd-$Pt_{85}Ni_{15}$ and $67\,m^2\,g_{Pt}^{-1}$ for fd-$Pt_{86}Ni_{14}$ based on the charge of the hydrogen underpotential deposition. Both values were comparable with that of commercial Pt/C ($68\,m^2\,g_{Pt}^{-1}$, 20 wt% Pt, Alfa Aesar) and higher than that of p-$Pt_{45}Ni_{55}$ ($52\,m^2\,g_{Pt}^{-1}$; Supplementary Fig. 5a).

Despite the similarity in composition, highly concave morphology and Pt skin, the ORR activity and stability of the sd-$Pt_{85}Ni_{15}$ and fd-$Pt_{86}Ni_{14}$ catalysts showed considerable differences. The sd-$Pt_{85}Ni_{15}$ catalysts displayed a high SA of $6.2 \pm 0.6\,mA\,cm^{-2}$ at 0.9 V versus RHE (Fig. 1h and Supplementary Fig. 5b), which was much higher than those of fd-$Pt_{86}Ni_{14}$ ($4.0 \pm 0.3\,mA\,cm^{-2}$), p-$Pt_{45}Ni_{55}$ ($2.7 \pm 0.2\,mA\,cm^{-2}$) and commercial Pt/C ($0.37 \pm 0.04\,mA\,cm^{-2}$). The sd-$Pt_{85}Ni_{15}$ showed a high MA of $4.0 \pm 0.4\,A\,mg_{Pt}^{-1}$, which was about 1.5 times that of fd-$Pt_{86}Ni_{14}$ ($2.6 \pm 0.2\,A\,mg_{Pt}^{-1}$), about 2.8 times that of p-$Pt_{45}Ni_{55}$ ($1.4 \pm 0.1\,A\,mg_{Pt}^{-1}$) and about 16.0 times that of Pt/C ($0.25 \pm 0.03\,A\,mg_{Pt}^{-1}$). Intriguingly, the durability of the sd-$Pt_{85}Ni_{15}$ and fd-$Pt_{86}Ni_{14}$ catalysts showed a more significant difference. After 20,000 cycles of ADT in O_2-saturated $HClO_4$, for sd-$Pt_{85}Ni_{15}$, the ECSA dropped by only 12%, the SA dropped by 9% and the MA dropped by only 21% (Fig. 1i and Supplementary Fig. 6a,b). These losses were much lower than those of the fd-$Pt_{86}Ni_{14}$ (47% in SA, 26% in ECSA and 61% in MA; Supplementary Fig. 7a,b) despite their similar compositions and morphologies. It was found that the composition of sd-$Pt_{85}Ni_{15}$ changed to sd-$Pt_{92}Ni_8$-ADT, and that that of fd-$Pt_{86}Ni_{14}$ changed to fd-$Pt_{95}Ni_5$-ADT (Supplementary Figs. 3 and 7d). Importantly, it was also found that sd-PtNi maintained the concave morphology after ADT without obvious size change (Supplementary Fig. 6c,d), whereas fd-PtNi transformed mostly into spherical nanoparticles (Supplementary Fig. 7c).

Development of BED and the Sabatier plot. To understand the structural details that render sd-$Pt_{85}Ni_{15}$ superior in activity and stability to fd-$Pt_{86}Ni_{14}$, we performed in situ X-ray absorption spectroscopy (XAS) studies. According to the in situ EXAFS spectra at the Pt L_3 edge (Supplementary Figs. 8–11 and Supplementary Table 1), the Pt–Pt bond lengths of both sd-$Pt_{85}Ni_{15}$ (2.71 Å) and fd-$Pt_{86}Ni_{14}$ (2.73 Å) are shorter compared to that of Pt/C (2.75 Å), resulting in strain and the improved SA over Pt/C. These results confirm that the Ni-induced compressive strain benefits the ORR activity. In addition, we found that after 20,000 cycles of ADT, the Pt–Pt bond

Fig. 1 | Design and comparison of sd-PtNi and fd-PtNi catalysts. a, Schematic illustration of the preparation of fd-PtNi catalyst and sd-PtNi catalyst from p-PtNi catalyst. **b**–**d**, Representative high-resolution atomic HAADF-STEM images for fd-$Pt_{86}Ni_{14}$ (**b**), p-$Pt_{45}Ni_{55}$ (**c**) and sd-$Pt_{85}Ni_{15}$ (**d**). The insets in **b**–**d** are the corresponding fast Fourier transform diffraction patterns. **e**–**g**, Corresponding EDX mapping and line-scan profile (following the direction of the white arrows) analysis for fd-$Pt_{86}Ni_{14}$ (**e**), p-$Pt_{45}Ni_{55}$ (**f**) and sd-$Pt_{85}Ni_{15}$ (**g**). **h**, Comparison of SA and MA values of p-$Pt_{45}Ni_{55}$, fd-$Pt_{86}Ni_{14}$ and sd-$Pt_{85}Ni_{15}$ catalysts at 0.9 V versus RHE. The error bars of all catalysts were determined from the standard deviation of ten individual measurements. **i**, Comparison of the retention of the ECSA, SA and MA of fd-$Pt_{86}Ni_{14}$ and sd-$Pt_{85}Ni_{15}$ catalysts at 0.9 V versus RHE, showing that sd-$Pt_{85}Ni_{15}$ has much better retention than fd-$Pt_{86}Ni_{14}$ in all aspects. **j**, The linear relationship between ln(SA/SA_{Pt}) and (−strain (%)) of the catalysts. The black dashed line is fitted without sd-$Pt_{85}Ni_{15}$ before ADT, showing a better agreement ($R^2 = 0.9$) than the grey dashed line with sd-$Pt_{85}Ni_{15}$ before ADT ($R^2 = 0.8$), suggesting the strain alone cannot fully account for the observed difference in SA of all the catalysts.

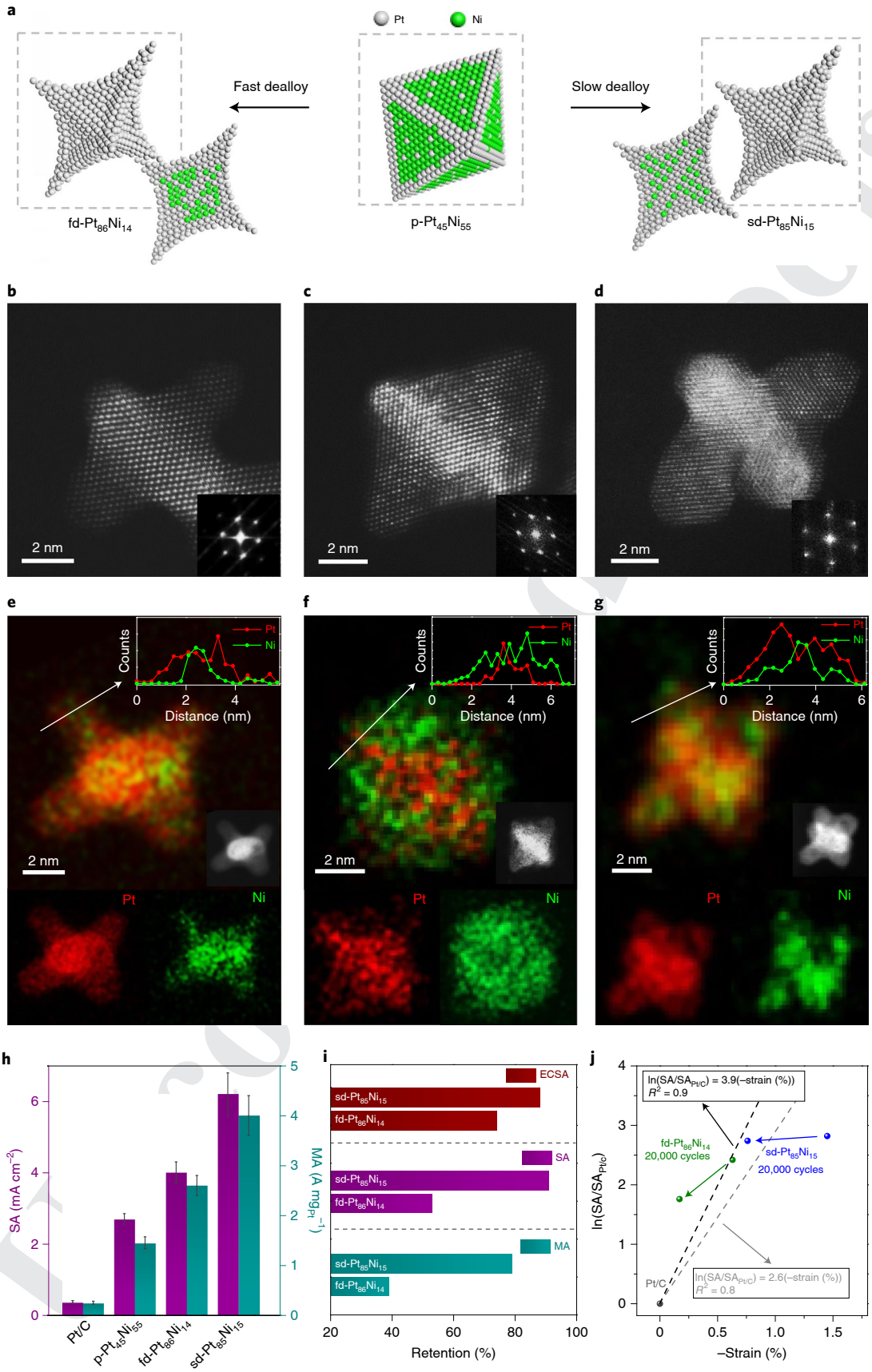
a
Pt
Ni
Fast dealloy
Slow dealloy
fd-Pt86Ni14
p-Pt45Ni55
sd-Pt85Ni15
b
c
d
2 nm
e
f
g
Counts
Distance (nm)
Pt
Ni
h
SA (mA cm−2)
MA (A mgPt−1)
Pt/C
p-Pt45Ni55
fd-Pt86Ni14
sd-Pt85Ni15
i
ECSA
SA
MA
Retention (%)
j
ln(SA/SAPt/C) = 3.9(–strain (%))
R2 = 0.9
fd-Pt86Ni14
20,000 cycles
sd-Pt85Ni15
20,000 cycles
ln(SA/SAPt/C) = 2.6(–strain (%))
R2 = 0.8
ln(SA/SAPt/C)
–Strain (%)

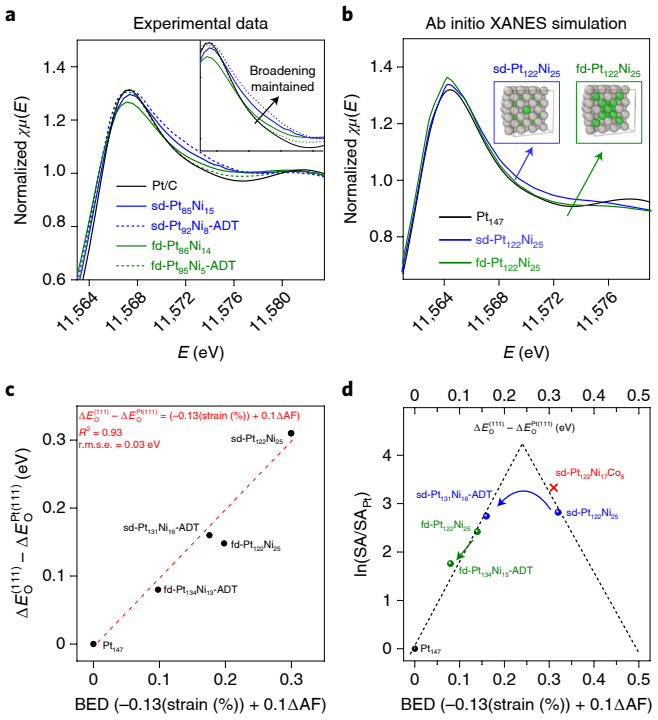

Fig. 2 | Development of the BED and the Sabatier plot. a, Experimental Pt L_3 edge in situ XANES spectra of sd-$Pt_{85}Ni_{15}$ (blue), sd-$Pt_{92}Ni_8$-ADT (blue-dashed), fd-$Pt_{86}Ni_{14}$ (olive) and fd-$Pt_{95}Ni_5$-ADT (olive-dashed) catalysts compared to Pt/C catalyst (black) collected at 0.54 V versus RHE in O_2-saturated 0.1 M $HClO_4$ solution. The inset panel is an enlarged region showing that the XANES broadening observed in sd-PtNi samples is maintained after ADT. **b**, Calculated Pt L_3 edge XANES spectra for Pt_{147} (black), sd-$Pt_{122}Ni_{25}$ (blue) and fd-$Pt_{122}Ni_{25}$ (olive) cluster models, showing similar broadening for sd-$Pt_{122}Ni_{25}$ models. The inset shows the cluster models of the sd-$Pt_{122}Ni_{25}$ and fd-$Pt_{122}Ni_{25}$ clusters. **c**, Linear regression fitting between the DFT-determined $\Delta E^{(111)}{}_O - \Delta E^{Pt(111)}{}_O$ and the BED (−0.13(strain (%)) + 0.1ΔAF) based on the cluster models, showing good one-to-one correspondence. r.m.s.e., root-mean-square error. **d**, The Sabatier-like relationship between experimentally measured activity (ln(SA/SA_{Pt})) of the Pt/C, sd-PtNi and fd-PtNi catalysts before and after 20,000 cycles of ADT and their corresponding simulated BED (−0.13(strain (%)) + 0.1ΔAF) based on cluster models. The top *x* axis is the DFT-determined difference of oxygen binding energy ($\Delta E^{(111)}{}_O - \Delta E^{Pt(111)}{}_O$). The red cross indicates the theoretically predicted high-performance sd-PtNiCo catalyst.

lengths of sd-$Pt_{85}Ni_{15}$ and fd-$Pt_{86}Ni_{14}$ relaxed to 2.73 Å and 2.75 Å, respectively (Fig. 1j and Supplementary Table 1). This Pt–Pt bond length relaxation indicates further dealloying and structural reorganization during ADT, which leads to the decrease in SA. However, we observed that although sd-$Pt_{85}Ni_{15}$ experienced Pt–Pt bond relaxation (2.71 Å to 2.73 Å) after ADT, its SA was largely maintained (from 6.2 ± 0.6 mA cm^{-2} to 5.6 ± 0.3 mA cm^{-2}) compared to that of fd-$Pt_{86}Ni_{14}$, whereas a Pt–Pt bond relaxation from 2.73 Å to 2.75 Å has led to a more drastic change in SA from 4.0 ± 0.3 mA cm^{-2} to 2.1 ± 0.3 mA cm^{-2}. Intriguingly, after ADT, sd-$Pt_{92}Ni_8$-ADT showed a considerably higher SA (5.6 ± 0.3 mA cm^{-2}) compared to that of the fd-$Pt_{86}Ni_{14}$ before ADT (4.0 ± 0.3 mA cm^{-2}), despite the same Pt–Pt bond length of 2.73 Å. This observation suggests that the Pt strain alone cannot fully account for the observed change in SA for sd-$Pt_{85}Ni_{15}$ before and after ADT. Indeed, the linear regression fittings between ln(SA/SA_{Pt}) and negative strain (%) of the catalysts suggest a much better fitting without sd-$Pt_{85}Ni_{15}$ before ADT ($R^2 = 0.9$) than with sd-$Pt_{85}Ni_{15}$ before ADT ($R^2 = 0.8$; Fig. 1j). This finding calls for a thorough investigation, especially on sd-$Pt_{85}Ni_{15}$, to capture contributing factors to the catalytic activity beyond simply strain.

A further examination of the sd-Pt alloys and fd-Pt alloys before and after ADT using in situ Pt L_3 XANES spectra revealed additional structural details that may contribute to the apparent difference in ORR activity and stability between the two classes of catalysts. Specifically, sd-$Pt_{85}Ni_{15}$ showed a considerable peak broadening in the energy range of 11,564 eV to 11,576 eV, compared to fd-$Pt_{86}Ni_{14}$ and commercial Pt/C (Fig. 2a), pointing to some unique atomic structural features achieved within the catalyst. XANES peak broadening was also observed for fd-$Pt_{86}Ni_{14}$, although to a much lower extent (Fig. 2a). However, after 20,000 cycles of ADT, the peak broadening remained prominent in sd-$Pt_{92}Ni_8$-ADT, while it was nearly gone in fd-$Pt_{95}Ni_5$-ADT (Fig. 2a). Together with the different catalyst morphologies after ADT in sd-PtNi (which remained a concave octahedra; Supplementary Fig. 6c) and in fd-PtNi (which turned spherical; Supplementary Fig. 7c), this observation suggests that the peak broadening in the Pt L_3 edge XANES spectra correlates with the fine structure of Pt alloys, which may be associated with structural stability. This broadening phenomenon has been observed, although little noted, in XAS studies of intermetallic Pt alloys featuring enriched charge transfer, such as ordered intermetallic PtFe (ref. [32]), PtNiCo (ref. [33]) and annealed PtCu (ref. [34]) and PtCo (ref. [35]). In particular, the Pt L_3 edge XANES peak area has been shown to reflect multiple scatterings involving both Pt and M neighbouring atoms and the change of density of states of the 5*d* orbitals, where its tailing to the higher energy indicates intensified Pt–M coupling[36–38]. In addition, we found that annealing the p-PtNi catalysts can also lead to a broad XANES peak (Supplementary Fig. 12) together with a high Pt–Ni coordination number (7 ± 1; Supplementary Table 2). We therefore infer that the XANES peak broadening observed in sd-$Pt_{85}Ni_{15}$ is associated with an intimate mixing of Ni and Pt in the catalysts that facilitates the charge transfer between the Pt and Ni (refs. [36,39]), denoting an intensified Pt–Ni coupling that weakens the Pt–O binding and in turn improves the intrinsic ORR activity of Pt (ref. [19]). We hypothesize that the drastic broadening and the resulting tailing of the in situ Pt XANES peak towards a higher energy, observed in sd-Pt alloys, may be a characteristic feature useful for representing Pt–M coupling that encompasses a ligand effect and local atomic coordination contribution to the ORR activities in Pt–M alloys in general.

To confirm this, we constructed 147-atom cuboctahedra cluster models based on the experimental data (Supplementary Fig. 13). In addition to a pure Pt_{147} cluster, we generated Pt–Ni clusters to represent fd-PtNi and sd-PtNi before and after ADT: a $Pt_{122}Ni_{25}$ cluster with Ni aggregated into the inner core and thus with the minimized number (204) of Pt–Ni nearest neighbour bonds to represent the fast-dealloying of peripheral Ni atoms in fd-$Pt_{86}Ni_{14}$, termed fd-$Pt_{122}Ni_{25}$; a fd-$Pt_{134}Ni_{13}$-ADT cluster with the minimized number of Pt–Ni bonds and a lower Ni content than fd-$Pt_{122}Ni_{25}$ to represent fd-$Pt_{95}Ni_5$-ADT; a sd-$Pt_{122}Ni_{25}$ cluster with 25 Ni and an intimate alloying of Ni and Pt in the particle core that thus maximizes the number (252) of Pt–Ni nearest neighbour bonds to represent the slow leaching together with atomic reordering of Ni into an energetically stable distribution in sd-$Pt_{85}Ni_{15}$; and a sd-$Pt_{131}Ni_{16}$-ADT cluster with the maximum number of Pt–Ni bonds but a lower Ni content than sd-$Pt_{122}Ni_{25}$ to represent sd-$Pt_{92}Ni_8$-ADT.

All clusters present a pure Pt skin. Density functional theory (DFT) geometry relaxation was performed on all structures (Methods). We then simulated XANES spectra via ab initio FEFF9 calculations[40] for the geometry-relaxed cluster models (Fig. 2b; raw data in the Supplementary Data). Notably, we observed a similar peak broadening in the simulated Pt L_3 XANES of the sd-Pt-alloy models with distributed Ni compared to Pt_{147} (Fig. 2b). By contrast,

no obvious peak broadening was observed in the fd-Pt-alloy models with aggregated Ni (Fig. 2b and Supplementary Fig. 14), consistent with experimental observations (Fig. 2a). A closer look into different sites in sd-$Pt_{122}Ni_{25}$ revealed that Pt sites featuring enriched Pt–Ni pairs showed obvious broadening, suggesting Pt–Ni coupling was in play (Supplementary Fig. 15c). The combined experimental (Fig. 2a) and computational (Fig. 2b and Supplementary Fig. 15) results so far confirmed the correlation between atomic Pt–Ni distribution in Pt alloys and Pt L_3 XANES peak broadening. Therefore, we suggest that Pt L_3 XANES peak broadening can be included in the activity descriptor for Pt-alloy nanocatalysts, together with the strain.

We use the peak AF (Methods and Supplementary Note 2 for details)[41] to represent the broadening in the Pt L_3 XANES peak, and further normalize the extent of the peak broadening among Pt-based catalysts to ΔAF ($\Delta AF = AF_{Pt\text{-}alloy} - AF_{Pt/C}$; Supplementary Table 3). We developed a BED descriptor (BED = A(strain (%)) + B(ΔAF); Supplementary Note 3) that can be used to represent the theoretical ΔE_O, which in turn determines the ORR activity (Supplementary Fig. 16). Through optimal linear regression fitting between the DFT-predicted BED ($\Delta E^{(111)}{}_O - \Delta E^{Pt(111)}{}_O$; Supplementary Tables 3–5) and the simulated BED on all 147-atom cuboctahedra cluster models, with strain extracted from relaxed cluster structures and the ΔAF from calculated XANES spectra, we arrived at BED = −0.13(strain (%)) + 0.1ΔAF. Significantly, the optimal fitted BED showed a good linear one-to-one correspondence relationship with the calculated $\Delta E^{(111)}{}_O - \Delta E^{Pt(111)}{}_O$, with high fidelity ($R^2 = 0.93$, root-mean-square error = 0.03 eV; Fig. 2c), which is a considerably better fitting than the strain-only descriptor ($R^2 = 0.82$, root-mean-square error = 0.04 eV; Supplementary Fig. 17). Notably, the ΔAF extracted from the simulated XANES spectra also showed a linear correlation with both the Pt–M coordination number (CN_{Pt-M}) (Supplementary Fig. 18a) and the $\Delta E^{(111)}{}_O - \Delta E^{Pt(111)}{}_O$ (Supplementary Fig. 18b), confirming the direct correlation between ΔAF and CN_{Pt-M} when there is peak broadening and its impact on O binding on the catalyst surface. We note that ΔAF is close to zero for the fd-PtNi models regardless of bulk/average CN_{Pt-Ni} (Supplementary Fig. 18a). Meanwhile our simulated XANES spectra showed vastly different broadening in Pt atoms at different locations within the same particle (Supplementary Fig. 15b) and that only sites with enriched Ni neighbours exhibit considerable broadening. We hence suggest that the AF of the XANES comprehensively reflects the Pt–M coupling, which includes both the contributions from composition (that is, average CN_{Pt-M}) and the local atomic contribution from M to Pt. There may exist a threshold value for local Ni content to demonstrate a significant peak broadening, similar to the observation made with a previous study on a well-defined Cu_xAu_{1-x} alloy[42]. Hence Pt–M coupling that leads to a noticeable change of the Pt *d*-band structure that modulates O binding on the Pt surface conveniently manifests in XANES peak broadening (ΔAF), making it a suitable experimental descriptor for ΔE_O.

We then plotted the experimental ORR activities with simulated BED, which demonstrated a clear Sabatier relationship, as one would expect for SA with the calculated $\Delta E^{(111)}{}_O - \Delta E^{Pt(111)}{}_O$, suggesting that these two can be used interchangeably (Fig. 2d). Interestingly, we found that sd-$Pt_{122}Ni_{25}$ resides at the right leg (weaker Pt–O binding) of the Sabatier plot, while the fd-$Pt_{122}Ni_{25}$ resides at the left leg (stronger Pt–O binding) of the plot (Fig. 2d). This observation may be used to explain the observed better stability for sd-$Pt_{122}Ni_{25}$: upon ADT, the $\Delta E^{(111)}{}_O$ of sd-PtNi decreases first, shifting the activity of sd-PtNi upward on the right slope passing the optimal peak position, and then downward along the left slope to the end position (Fig. 2d, blue points), resulting in little change in activity despite a large change in $\Delta E^{(111)}{}_O$. By comparison, the fd-$Pt_{122}Ni_{25}$ starts on the left leg of the Sabatier plot, and its activity decreases monotonically with the decreasing $\Delta E^{(111)}{}_O$ caused by strain relaxation (Fig. 2d, olive points).

The well-acknowledged instability of Pt–M ORR catalysts has been attributed to the leaching of M, which leads to the changes in both composition and structure that result in relaxed Pt–Pt strain and the electronic Pt–M ligand effect[21,43]. Hence, in order to retain the high activity of Pt–M catalysts, it is essential to develop a catalyst with robustness in both composition and atomic structure[26,44,45], since these parameters are intimately related to the activity of the catalyst. Indeed, our calculations also showed better thermodynamic stability for sd-$Pt_{122}Ni_{25}$ with a mixing energy[46] of −13.27 eV (Methods) than for fd-$Pt_{122}Ni_{25}$ (mixing energy of −12.24 eV; Supplementary Fig. 19), consistent with experimental observations of the shape retention in sd-PtNi-ADT but not in fd-PtNi-ADT, suggesting less atomic movement. The calculation also showed that the presence of enriched subsurface Ni, particularly in the slow-dealloyed structures, significantly weakens the interaction between the oxygen and the undercoordinated Pt vertex sites (Supplementary Figs. 20 and 21). The $\Delta E^{(Vertex)}{}_O - \Delta E^{Pt(Vertex)}{}_O$ (Supplementary Tables 3–5), defined as the difference between the $\Delta E^{(Vertex)}{}_O$ of the Pt alloy and the $\Delta E^{Pt(Vertex)}{}_O$ of the Pt at the vertex site, increases from 0.15 eV for fd-$Pt_{122}Ni_{25}$ alloy to 0.21 eV for sd-$Pt_{122}Ni_{25}$ alloy, suggesting weaker Pt–O binding on sd-PtNi vertex sites. The weaker Pt–O binding on these vulnerable sites protects them and increases their stability under reaction conditions[47,48]. In addition, an even weaker Pt–O binding ($\Delta E^{(Vertex)}{}_O - \Delta E^{Pt(Vertex)}{}_O = 0.28$ eV) was found on $L1_0$-$Pt_{116}Ni_{31}$ structure (Supplementary Figs. 20 and 21), representing the more stable intermetallic phase (Supplementary Fig. 21), confirming this trend that thermodynamic stability leads to better structure stability and hence ORR stability. Together, based on this experimental Sabatier plot, we can expect that Pt-alloy catalysts with large strain and AF tend to reside on the right side of the plot showing better stability, while those sitting closer to the top of the right slope may exhibit simultaneous high activity and high stability.

ORR catalyst design based on BED. Taking a step further, we constructed a ternary sd-$Pt_{122}Ni_{17}Co_8$ model (Methods and Supplementary Fig. 13) due to the higher chemical stability of ternary PtNiCo[30,49,50]. For sd-$Pt_{122}Ni_{17}Co_8$, our model predicted a $\Delta E^{(111)}{}_O - \Delta E^{Pt(111)}{}_O$ of 0.30 eV, with a corresponding BED value of 0.30, which sits closer to the optimal position of the calculated Sabatier plot (red cross points, Fig. 2d) and demonstrates a better thermodynamic stability (calculated mixing energy of −15.11 eV; Supplementary Fig. 19). Thus, we expected that sd-$Pt_{122}Ni_{17}Co_8$ should outperform sd-$Pt_{122}Ni_{25}$ in terms of both ORR activity and stability (Fig. 2d).

We then synthesized concave PtNiCo catalyst following a similar protocol as that established for sd-$Pt_{85}Ni_{15}$ and obtained PtNiCo catalysts with a similar morphology and Pt composition, which were termed sd-$Pt_{84}Ni_{12}Co_4$ catalysts (Methods and Supplementary Figs. 22–26). As predicted, the sd-$Pt_{84}Ni_{12}Co_4$ showed Pt L_3 XANES peak broadening (Fig. 3a) and compressive strain (Fig. 3b and Supplementary Figs. 27 and 28). Similar to sd-$Pt_{85}Ni_{15}$, the peak broadening (AF) and the concave morphology of sd-$Pt_{84}Ni_{12}Co_4$ were maintained even after the 20,000 cycles of ADT (Fig. 3a,f and Supplementary Fig. 26c). As predicted, sd-$Pt_{84}Ni_{12}Co_4$ demonstrated superior activity to sd-$Pt_{85}Ni_{15}$ (Fig. 3c,d and Supplementary Fig. 25). Specifically, sd-$Pt_{84}Ni_{12}Co_4$ showed an impressive SA of 10.7 ± 1.4 mA cm^{-2} and MA of 7.1 ± 1.0 A mg_{Pt}^{-1} at 0.9 V versus RHE, which are 28.9 times and 28.4 times, respectively, those of Pt/C (Supplementary Fig. 25b and Supplementary Table 6). Based on the experimentally determined BED and the activity of sd-$Pt_{84}Ni_{12}Co_4$, we found that the sd-$Pt_{84}Ni_{12}Co_4$ was indeed located near the top right of the Sabatier plot (Fig. 3c). Significantly, the SA of the designed sd-$Pt_{84}Ni_{12}Co_4$ is highly competitive among state-of-the-art Pt-based catalysts, including Mo-doped Pt_3Ni (ref. [51]) and state-of-the-art jagged Pt nanowires (J-PtNWs;[27] Fig. 3d,g). More importantly, the sd-$Pt_{84}Ni_{12}Co_4$ also showed simultaneously

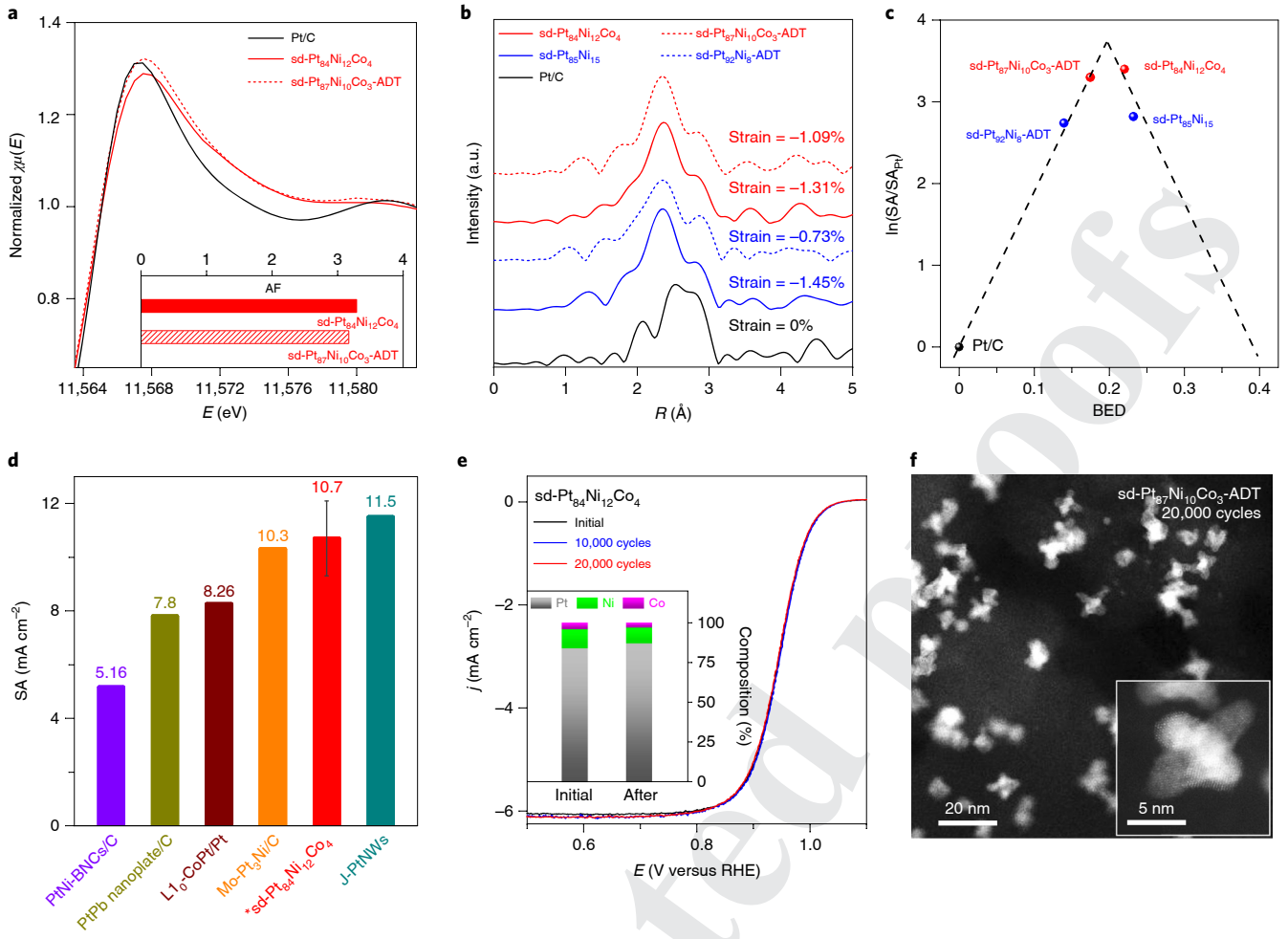

g

Catalyst	SA (mA cm^{-2})		ADT cycles	SA retention (%)	ECSA (m^2 g^{-1})	MA (A mg^{-1})
	BOL	ADT				
sd-$Pt_{84}Ni_{12}Co_4$ (this work)	10.7	10.1	20,000	95	68	7.1
sd-$Pt_{85}Ni_{15}$ (this work)	6.2	5.6	20,000	91	65	4.0
fd-$Pt_{86}Ni_{14}$ (this work)	4.0	2.1	20,000	53	65	2.6
PtNi-BNCs/C	5.16	5.17	50,000	100.2	68.2	3.52
PtPb nanoplate/C	7.8	7	50,000	89	55	4.3
Pt_3Ni/C nanoframes	8.4*	NA	10,000	NA	67.2	5.7
$L1_0$-CoPt/Pt	8.26	6.77	30,000	82	27.3	2.26
J-PtNWs/C	11.5	10.8	6,000	94.5	118	13.6

Fig. 3 | Experimentally validated sd-PtNiCo catalyst with high activity and stability. a, Pt L_3 edge in situ XANES spectra of sd-$Pt_{84}Ni_{12}Co_4$ (red) and sd-$Pt_{87}Ni_{10}Co_3$-ADT (red-dashed) compared to Pt/C catalyst (black) collected at 0.54 V versus RHE in O_2-saturated 0.1 M $HClO_4$ solution. The inset is the AF of the concave sd-PtNiCo catalyst before and after ADT. **b**, In situ Fourier transform of EXAFS spectra of sd-$Pt_{84}Ni_{12}Co_4$ (red), sd-$Pt_{87}Ni_{10}Co_3$-ADT (red-dashed), sd-$Pt_{85}Ni_{15}$ (blue), sd-$Pt_{92}Ni_8$-ADT (blue-dashed) and Pt/C (black). In situ data were collected in an O_2-purged 0.1 M $HClO_4$ electrolyte at 0.54 V versus RHE. **c**, The relationship between experimentally measured activity (ln(SA/SA_{Pt})) and BED of sd-$Pt_{84}Ni_{12}Co_4$, sd-$Pt_{87}Ni_{10}Co_3$-ADT, sd-$Pt_{85}Ni_{15}$, sd-$Pt_{92}Ni_8$-ADT and Pt/C catalyst, showing a similar trend to the simulation. The dashed line is adopted from the literature[6] with BED replacing $\Delta E_O - \Delta E^{Pt}{}_O$ on the *x* axis. **d**, Comparison of SA values at 0.9 V versus RHE for sd-$Pt_{84}Ni_{12}Co_4$ from this work (labelled with *) and other state-of-the-art ORR catalysts: PtNi-BNCs/C (ref. [26]), PtPb nanoplate/C (ref. [25]), $L1_0$-CoPt/Pt (ref. [45]), Mo-Pt_3Ni/C (ref. [51]) and J-PtNWs (ref. [27]). The error bars of all catalysts were determined from the standard deviation of ten individual measurements. **e**, ORR polarization curves for the sd-$Pt_{84}Ni_{12}Co_4$ before ADT (black), after 10,000 cycles of ADT (blue) and after 20,000 cycles of ADT (red) between 0.6 and 1.0 V versus RHE, showing little loss in activity. Inset is the EDX-determined composition comparison before and after 20,000 cycles of ADT. **f**, HAADF-STEM image of sd-$Pt_{87}Ni_{10}Co_3$-ADT after 20,000 cycles of ADT; inset shows the high-resolution STEM image. **g**, Performance of fd-$Pt_{86}Ni_{14}$, sd-$Pt_{85}Ni_{15}$ and sd-$Pt_{84}Ni_{12}Co_4$ catalysts, in comparison to those in several representative works: PtNi-BNCs/C (ref. [26]), PtPb nanoplate/C (ref. [25]), Pt_3Ni/C nanoframes (ref. [63]), $L1_0$-CoPt/Pt (ref. [45]) and J-PtNWs/C (ref. [27]). All activities were compared at 0.9 V versus RHE. BOL, beginning of life; *, calculated based on reported data; NA, not available.

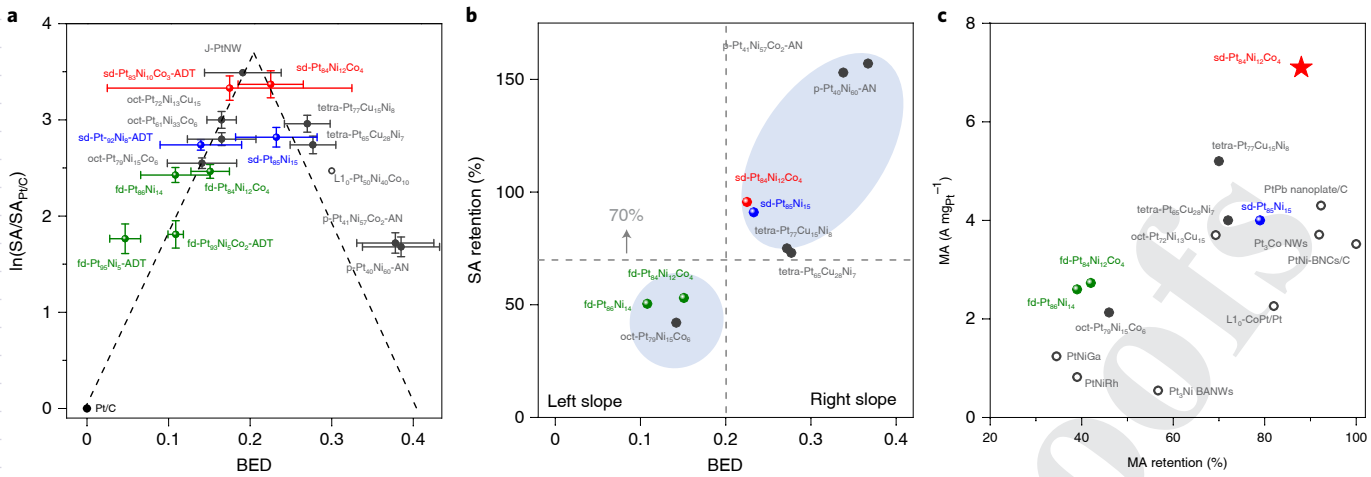

Fig. 4 | Experimentally validated Sabatier plot of Pt-alloy catalysts and stability analysis. a, Experimental Sabatier plot of Pt-alloy catalysts. The Supplementary Information describes the preparation of the tetra-PtCuNi, fd-PtNiCo, p-PtNi-AN and p-PtNiCo-AN catalysts. Hollow circles represent catalysts reported in the literature: L1$_0$-Pt$_{50}$Ni$_{40}$Co$_{10}$ (ref. [33]), J-PtNWs (ref. [27]), oct-Pt$_{72}$Ni$_{13}$Cu$_{15}$ (ref. [44]) and oct-Pt$_{61}$Ni$_{33}$Co$_6$ (composition was determined before activation)[50]. The dashed line is adopted from the literature[6] with BED replacing $\Delta E_O - \Delta E^{Pt}{}_O$ on the *x* axis. The error bars of BED consist of the uncertainties of strain from the EXAFS fitting and the uncertainties of ΔAF measured in ten XANES spectra. The activity error bars were determined from the standard deviation of ten individual measurements. **b**, Comparison of SA retention for left-slope catalysts and right-slope catalysts after 20,000 cycles of ADT between 0.6 V and 1.0 V versus RHE at a sweep rate of 100 mV s^{-1} in O_2-saturated 0.1 M $HClO_4$. The vertical dashed line is the separation line of the left slope and right slope. **c**, MA and MA retention of Pt-alloy catalysts (with at least 20,000 cycles of ADT), suggesting that sd-PtNiCo (labelled with a red star) possesses both high MA and high MA retention. Hollow circles represent catalysts reported in the literature: PtPb nanoplate/C (ref. [25]), PtNi-BNCs/C (ref. [26]), L1$_0$-CoPt/Pt (ref. [45]), oct-Pt$_{72}$Ni$_{13}$Cu$_{15}$ (ref. [44]), Pt$_3$Ni BANWs (ref. [64]), PtNiRh (ref. [65]), PtNiGa (ref. [66]) and Pt$_3$Co NWs (ref. [67]).

exceptional stability with only 8% loss of ECSA, 5% loss of SA and 12% loss of MA after the ADT (Fig. 3e, Supplementary Fig. 26b and Supplementary Table 6), all superior to thae values of sd-Pt$_{85}$Ni$_{15}$, as predicted. The composition of the sd-Pt$_{84}$Ni$_{12}$Co$_4$ stayed essentially unchanged after 20,000 cycles of ADT (inset of Fig. 3e and Supplementary Fig. 23), and the concave morphology of sd-Pt$_{84}$Ni$_{12}$Co$_4$ was also largely maintained (Fig. 3f and Supplementary Fig. 26c; the percentage of concave shape is 78% in comparison to 88% before ADT). Importantly, the broadening was also observed on ex situ samples (Supplementary Fig. 29), making the BED more practical to obtain and apply in catalyst performance prediction experimentally.

Our proposed BED thus fully accounts for the experimentally observed ORR activities for sd-Pt alloys and fd-Pt alloys before and after ADT (Fig. 3c), which leads to an experimental Sabatier plot to predict the Pt-alloy activity (SA) based on the experimentally measurable value −0.13(strain (%)) + 0.1ΔAF. On this experimental Sabatier plot, the sd-Pt alloys started on the right slope before the ADT, and both were on the left slope after the ADT. During this process, the strain and the Pt–M coupling (the local coordination environment that contributed to the broadening of the Pt L_3 edge in situ XANES spectra) might work synergistically to preserve the activity of the Pt alloys. Hence, Pt alloys with such a feature may still maintain a $\Delta E^{(111)}{}_O$ closer to the optimal value despite the lattice relaxation during the long-term electrocatalytic reactions, exhibiting robust stability. This observation suggests that Pt-alloy catalysts whose BED lies on the right slope of the Sabatier plot, usually those with large strain and/or ΔAF, may exhibit better stability than those with a BED on the left.

Discussion

To examine the universality of the descriptor, we examined various Pt-alloy catalysts (Supplementary Information for the synthesis details) with different morphologies, structures and compositions (Supplementary Tables 2 and 3 and Supplementary Figs. 30–32). With the experimentally measured activity ln(SA$_{Pt\text{-}alloy}$/SA$_{Pt/C}$) as the *y* axis, and the BED in place of $\Delta E^{(111)}{}_O - \Delta E^{Pt(111)}{}_O$ on the *x* axis, we found that all examined catalysts fall nicely into the predicted Sabatier relation (Fig. 4a). As shown in the plot, the Pt-based catalysts without XANES broadening (or a negligible ΔAF) all reside at the left side of the Sabatier plot, including the previously reported J-PtNWs, which sit near the top left of the plot (Fig. 4a). The intermetallic Pt alloy (extracted from the literature[33]), the tetrahedral PtCuNi alloys (tetra-PtCuNi) and the annealed p-Pt alloy (p-Pt-alloy-AN) all reside on the right slope of the Sabatier plot, showing considerable broadening in their Pt L_3 XANES peaks and large strain. We expect that this BED can predict ORR activities for virtually all Pt-based catalysts without prior knowledge of the composition, morphology or structure. We also expect that this BED can be used to qualitatively predict the stability of Pt-alloy catalysts, based on which side of the slope they reside on. We hypothesize that similar to sd-PtNi and sd-PtNiCo, Pt alloys located on the right side of the experimental Sabatier plot may demonstrate higher stability than those on the left. We further investigated the stability (20,000 cycles of ADT) of the catalysts on the left slope and the right slope (Fig. 4b). As expected, the catalysts located on the right slope of the experimental Sabatier plot all showed an excellent SA retention above 70%, including sd-Pt alloys, tetra-PtCuNi and the annealed p-PtNi-AN and p-PtNiCo-AN. Interestingly, the p-PtNi-AN and p-PtNiCo-AN located at the lower side of the right slope showed an even higher SA after ADT than that at which they started (retention about 150%; Supplementary Fig. 31i–l), indicating that ADT decreased BED (and hence $\Delta E_O - \Delta E^{Pt}{}_O$) and shifted the SA up the right side of the Sabatier plot. By contrast, those Pt-alloy catalysts located at the left slope usually showed a lower SA retention around 50%, consistent with the expectation. Therefore, the BED can capture the contributions from both the strain effect and Pt–M coupling effect to reflect the calculated oxygen binding energy ($\Delta E_O - \Delta E^{Pt}{}_O$) in Pt-alloy catalysts, and can be used to predict both the activity and stability of ORR catalysts. We expected that the Pt alloys located near the top of the right slope may present the most desirable ORR catalysts, possessing both high SA and high stability,

such as the sd-PtNiCo we designed in this study. In addition to a large and stable ECSA, the sd-PtNiCo showed a simultaneous high MA of 7.1 ± 1.0 A mg_{Pt}^{-1} and MA retention of 88%, showing the optimal combination of activity and stability among the state-of-the-art ORR catalysts (Fig. 4c). Importantly, the excellent ORR performance of sd-PtNiCo has also been realized in a membrane electrode assembly, suggesting its applicability in a practical fuel cell. The sd-PtNiCo exhibited a high MA of 0.67 ± 0.03 A mg_{Pt}^{-1} and considerable MA retention of 64% after 30,000 square wave cycles of accelerated stress tests at a cathode loading of 0.083 mg_{Pt} cm^{-2} (Methods and Supplementary Figs. 33 and 34).

In summary, by comparing the structure–function relationship of concave octahedral sd-PtNi and fd-PtNi catalysts, we found that compressive strain and Pt–Ni coupling can be cumulatively captured with a BED descriptor ($BED = -0.13(\text{strain}\ (\%)) + 0.1\Delta AF$) that can be used in a way similar to the DFT-calculated ΔE_O to predict the ORR activity of Pt-alloy catalysts. The BED works generally well to describe the experimentally observed ORR activities for Pt-alloy catalysts, confirming a Sabatier relation that can be used to predict both the activity and the stability of the Pt-based ORR catalysts. Based on this BED, we designed a sd-$Pt_{84}Ni_{12}Co_4$ catalyst residing near the top of the right leg of the Sabatier plot, which exhibited a simultaneously high SA of 10.7 ± 1.4 mA cm^{-2} and excellent stability, showing only 8% loss of ECSA, 5% loss of SA and 12% loss of MA after 20,000 cycles of ADT. The high activity and stability of the sd-PtNiCo catalysts have also been validated in a membrane electrode assembly, with both MA and stability surpassing targets set by the US Department of Energy.

Methods

Chemicals. Platinum(II) acetylacetonate ($Pt(acac)_2$, 97%), nickel(II) acetylacetonate ($Ni(acac)_2$, 95%), cobalt(II) acetylacetonate ($Co(acac)_2$, 97%), copper(II) acetylacetonate ($Cu(acac)_2$, 97%), perchloric acid ($HClO_4$, 70%, parts per 10^{12} (ppt) grade), glucose, benzoic acid (C_6H_5COOH, ≥99.5%), oleylamine (OAm; $CH_3(CH_2)_7CH{=}CH(CH_2)_7CH_2NH_2$, >70%), 1-octadecene (ODE; $CH_2{=}CH(CH_2)_{15}CH_3$; technical grade, >90%) and 5 wt% Nafion were all purchased from Sigma-Aldrich. Commercial Pt/C catalyst (20 wt% Pt, particle size 2 to 5 nm), Pt/C catalyst (10%) and Pt/C catalyst (40%) were purchased from Alfa Aesar. DMF (≥99.8%), ethanol (200 proof) and cyclohexane (C_6H_{12}; analytical reagent, >99.5%) were obtained from EMD Millipore and Decon. Acetone (≥99.5%) and isopropanol (≥99.5%) were purchased from Fisher Scientific. All reagents were used as received without further purification. Carbon black (Vulcan XC-72) was received from Carbot Corporation and annealed in 280 °C air before use. Deionized water (18 MΩ cm^{-1}) was obtained from an ultra-pure purification system (Milli-Q Advantage A10). The Nafion HP membrane and gas diffusion electrode were purchased from Fuel Cell store.

Preparation of p-Pt-alloy catalysts. In a typical synthesis of p-$Pt_{45}Ni_{55}$ catalysts, 10 mg $Pt(acac)_2$, 20 mg $Ni(acac)_2$ and 250 mg benzoic acid were added to 10 ml of a solution of carbon black suspended in DMF (total 30 mg carbon black) in a 35 ml glass vial. The mixture was ultrasonicated for 10 minutes, heated to 160 °C and kept at that temperature for 12 hours with stirring in an oil bath. After reaction, the vial was cooled to room temperature; the p-$Pt_{45}Ni_{55}$ catalyst was obtained by centrifugation, washed with an isopropanol/acetone mixture several times and dried in a vacuum dryer. The synthesis of p-$Pt_{41}Ni_{54}Co_5$ octahedra was similar to the above protocol except an additional 5 mg $Co(acac)_2$ was added.

Preparation of sd-Pt-alloy catalysts. First, 200 mg p-Pt-alloy catalysts was dissolved with 150 ml DMF in a 250 ml three-neck flask and sonicated for 20 minutes. Then, the three-neck flask with stirring was put into the oil bath and heated to 120 °C. The solution was purged with air and refilled with DMF to maintain a constant level of solution. The sample was collected at different times, centrifuged and washed with an isopropanol/acetone mixture. The resulting sd-Pt alloy was further dried in a vacuum dryer.

Preparation of fd-Pt-alloy catalysts. The preparation of fd-Pt-alloy catalysts was achieved by annealing p-Pt-alloy catalysts in air at 120 °C for 2 hours to mimic the annealing condition of sd-Pt-alloy catalysts. Then, the annealed catalysts were dealloyed in 0.5 M H_2SO_4 at 80 °C for 2 hours. The sample was collected by centrifugation and then washed with deionized water until the pH was neutral. The resulting fd-Pt-alloy catalysts were further dried in a vacuum dryer.

Preparation of tetrahedra PtCuNi catalysts. The synthesis of tetrahedra PtCuNi (tetra-PtCuNi) catalysts is based on a previous report[52]. In a typical synthesis of tetra-$Pt_{77}Cu_{15}Ni_8$ catalysts, $Pt(acac)_2$ (20 mg), $Cu(acac)_2$ (6 mg), $Ni(acac)_2$ (6 mg), glucose (135 mg), OAm (3 ml) and ODE (2 ml) were added to a 35 ml vial. The mixture was ultrasonicated for 1 hour, purged with carbon monoxide (CO) for 5 minutes and heated to 170 °C in 0.5 h and kept for 12 h in an oil bath with stirring. After cooling to room temperature, the colloidal products were collected and washed with a cyclohexane/ethanol mixture (v/v = 1:5) two times. The synthesis of tetra-$Pt_{65}Cu_{28}Ni_7$ was similar to the above protocol except an additional 12 mg $Ni(acac)_2$ was used. The as-prepared tetra-PtCuNi catalysts were dispersed in a 20 ml cyclohexane/ethanol mixture (v/v = 1:1) containing carbon black (20 mg) and sonicated for 2 hours. The resulting catalysts were collected by centrifugation and washed with a cyclohexane/ethanol mixture. After drying, the catalysts were annealed at 130 °C for 6 hours in Ar (100 sccm) in a home-built tube furnace. The composition was determined by EDX after the catalysts were activated.

Preparation of p-Pt-alloy-AN catalysts. The p-PtNi-AN and p-PtNiCo-AN catalysts were prepared by annealing the p-PtNi and p-PtNiCo catalysts in a home-made furnace at 700 °C for 2 hours with a mixture of gas flow (Ar/H_2 = 300 sccm:3 sccm).

Preparation of octahedral $Pt_{79}Ni_{15}Co_6$ catalysts. The synthesis of octahedral $Pt_{79}Ni_{15}Co_6$ (oct-$Pt_{79}Ni_{15}Co_6$) catalysts is similar to the method in a previous report[30]. In short, 10 mg $Pt(acac)_2$, 5 mg $Ni(acac)_2$, 5 mg $Co(acac)_2$ and 65 mg benzoic acid were added to 10 ml of a solution of carbon black suspended in DMF (total 30 mg carbon black) in a 35 ml glass vial. The vial was then capped and ultrasonically processed for 20 minutes, followed by heating with magnetic stirring in an oil bath at 160 °C for 12 hours. After reaction, the vial was cooled to room temperature. The oct-$Pt_{79}Ni_{15}Co_6$ catalyst was obtained by centrifugation and washed with an isopropanol/acetone mixture several times. The resulting catalyst was dried in a vacuum dryer.

Structure and composition characterization. Powder X-ray diffraction patterns were collected on a Panalytical X'Pert Pro X-ray powder diffractometer with Cu Kα radiation. Low-magnification TEM images were taken on a FEI T12 transmission electron microscope operated at 120 kV. High-resolution TEM images, EDX line-scan files and HAADF-STEM images were taken on a JEM-ARM300F Grand ARM operated at 300 kV. TEM samples were prepared by dropping an ethanol dispersion of catalysts onto carbon-coated aluminium TEM grids. The Pt loading of catalysts was determined by inductively coupled plasma atomic emission spectroscopy. The Pt loading was determined before electrochemical measurement. The Pt loading is about 10.6 wt% for p-Pt alloys and about 9.5 wt% for sd-Pt alloy and fd-Pt alloys.

Electrochemical measurement. A three-electrode cell system was used to conduct all electrochemical tests. The working electrode was a glassy carbon rotating disc electrode with a 0.196 cm^2 glassy carbon geometry area, from Pine Instruments. The counter and reference electrodes were Pt wire and Ag/AgCl (1 M Cl^-), respectively. For activity measurement, Pt loadings were 7.85 μg cm^{-2}, 7.65 μg cm^{-2}, 5.65 μg cm^{-2} and 5.55 μg cm^{-2} for p-$Pt_{45}Ni_{55}$, p-$Pt_{41}Ni_{54}Co_5$, sd-$Pt_{85}Ni_{15}$ and sd-$Pt_{84}Ni_{12}Co_4$, respectively. The Pt loadings of fd-Pt alloy and Pt/C catalysts were about 7.5 μg cm^{-2} and 10 μg cm^{-2}, respectively. Cyclic voltammetry activations were performed in N_2-saturated 0.1 M $HClO_4$ electrolyte with a potential scan rate of 100 mV s^{-1} from 0.05 to 1.1 V versus RHE, until cyclic voltammetry curves stabilized. The ECSA was determined by integrating the hydrogen underpotential deposition area (H_{upd}) on the cyclic voltammetry curve by taking a value of 210 μC cm^{-2} for the adsorption of a hydrogen monolayer. The ORR was tested in an O_2-saturated 0.1 M $HClO_4$ electrolyte with a potential scan rate of 20 mV s^{-1}. The measurement temperature was set at 25 °C using a water bath five-neck flask. The current density of the ORR polarization curves was *iR* corrected and background corrected. The ADT were performed at room temperature in O_2-saturated 0.1 M $HClO_4$ solutions by applying cyclic voltammetry sweeps between 0.6 and 1.0 V versus RHE at a sweep rate of 100 mV s^{-1}.

Membrane electrode assembly preparation and single fuel cell test. The single fuel cell performance of the catalysts as the cathode was tested with an 850e Fuel Cell Test System (Scribner). The membrane electrode assemblies with an active area of 5.0 cm^2 were fabricated using the catalyst-coated membrane method. The anode loading was set to be 0.025 mg_{Pt} cm^{-2} (10% Pt/C, Alfa Aesar). Catalysts were incorporated into membrane electrode assemblies by direct spraying of a water/2-propanol-based ink onto a Nafion HP membrane with a loading of 0.083 mg_{Pt} cm^{-2}. The mass activity was measured via measuring the current at 0.9 $V_{iR\text{-}free}$ under 150 kPa_{abs} H_2/O_2 (80 °C, 100% relative humidity, H_2/O_2 = 835:2,000 sccm) with H_2 crossover correction. The potential cycling accelerated stress tests were conducted using the square wave method from 0.6 V to 0.95 V with 3 s hold time at each potential (150 kPa_{abs} H_2/N_2, 80 °C, 100% relative humidity, H_2/N_2 = 100:100 sccm). The H_2/air test was conducted under 250 kPa_{abs} H_2/air (94 °C, 100% relative humidity, H_2/air = 1.5:1.8 stoi, 126:358 sccm).

XAS data collection and analysis. The electrode inks for the XAS electrodes were similar to the rotating disc electrode. The ink was drop-cast onto a carbon paper with a total catalyst loading of about 8 mg cm^{-2}. For convenience, examined catalysts were activated on the three-electrode system prior to XAS measurements. The ADT samples were cycled following the same protocol as on the rotating disc electrode. The XAS experiments were conducted at room temperature in a previously described in situ spectro-electrochemical half cell in which a continuously O_2-purged 0.1 M $HClO_4$ aqueous solution was circulated[53], at beamlines ISS 6-BM and 8-ID at the National Synchrotron Light Source II (Brookhaven National Laboratory, NY). Before transfer into the cell, the electrodes were conditioned in 0.1 M $HClO_4$ under vacuum for 40 minutes to remove surface oxides and contaminants. Potentiostatic control was maintained with an Autolab PGSTAT30 potentiostat (Metrohm USA, formerly Brinkman Instruments). Full-range Pt L_3 edge, Ni K edge and/or Co K edge spectra were taken at various static potentials along the anodic sweep of the cyclic voltammetry. Data were collected on the same electrode in transmission mode at the Pt L_3 edge, and fluorescence mode at the Ni and/or Co K edge, with a Pt/Co/Ni reference foil positioned between the ionization chambers I2 and I3 as a reference. The voltage cycling limits were 0.05 to 1.00 V versus RHE. Data collection was performed at the chosen potentials held during anodic sweeps. The electrode was fully cycled following each potential hold to clean the electrode surfaces after each potential hold. Typical experimental procedures were utilized with details provided in our previous work[43]. The data were processed and fitted using the IFEFFIT-based Athena[54] and Artemis[55] programs. Scans were calibrated, aligned and normalized with background removed using the IFEFFIT suite[56]. The $\chi(R)$ were modelled using single scattering paths calculated by FEFF6 (ref. [57]).

By comparison, traditional first-shell EXAFS analysis was performed on studied samples with similar parameter settings. The fits were conducted at the Pt L_3 and Ni K edges concurrently for beginning of life samples, but for ADT samples the fits were conducted only at the Pt L_3 edge since the Ni is in a mixed, formed metal and oxidative phases and cannot be fitted. The fitting results are listed in Supplementary Table 1. A Pt_3Ni_1 face-centered cubic cluster model was used for EXAFS fitting. The first-shell Pt–Pt and Pt–Ni paths and Ni–Pt and Ni–Ni paths were included for fitting at the Pt L_3 edge and Ni K edge, respectively. Basic constraints $R_{Pt\text{-}Ni} = R_{Ni\text{-}Pt}$ and $\sigma^2_{Pt\text{-}Ni} = \sigma^2_{Ni\text{-}Pt}$ were introduced during the fitting. Here $R_{Pt\text{-}Ni}$ ($R_{Ni\text{-}Pt}$) is the bond distance for Pt–Ni (Ni–Pt) scattering, and $\sigma^2_{Pt\text{-}Ni}$ ($\sigma^2_{Ni\text{-}Pt}$) is the D-E factor of the bond lengths given by the fitting. Owing to the low content of Co in the sd-PtNiCo catalyst and the fact that Ni and Co cannot be distinguished by XAS as scattering neighbours, these restrictions were applied for the sd-PtNiCo as well.

Computational studies. The XANES spectra were simulated by employing the FEFF9 code[57], which calculates the self-consistent multiple scattering from atomic targets whose scattering potential is obtained by overlapping free atom densities in the muffin tin approximation[58]. We calculated the Pt L_3 edge structure for 147-atom cuboctahedral cluster models as described below and depicted in Supplementary Fig. 13, and we reported them, usually averaged over all atoms. Simulated XANES spectra of individual Pt atoms are also reported in the main text.

Quantum mechanical DFT calculations were performed on PtNi clusters of up to 147 atoms in size. For each cluster model, full local geometry relaxation was performed starting from the geometry of Pt_{147}. We used the Quantum Espresso[59] suite of programs, the Perdew–Burke–Ernzerhof[60] exchange–correlation functional and ultra-soft pseudopotentials[61]. Local geometry optimizations were performed spin unrestricted and employed the following numerical parameters: wavefunction and charge-density cut-offs equal to 40 and 400 Ry, respectively, a simple cubic cell with side length of 20 a.u., a Gaussian smearing of the one-electron energy levels of 0.001 a.u., a convergence threshold for self-consistency equal to 0.5×10^{-6} a.u. and a reciprocal space sampled at the gamma point only. Geometries were considered to be converged when the forces on each atom became smaller than 0.001 a.u.

The models investigated in this work are based on a 147-atom cluster of cuboctahedral symmetry (Supplementary Fig. 13). Atoms in this cluster can be distinguished into nine symmetry-equivalent groups or orbits[46]: one atom at the centre (orbit (i)), a first shell of 12 first neighbours (orbit (ii)), six atoms on subsurface (100) facets (orbit (iii)), 24 atoms on subsurface (111) facets (orbit (iv)), 12 atoms on subsurface vertexes (orbit (v)), eight atoms on (111) surface facets (orbit (vi)), 24 atoms on (100) surface facets (orbit (vii)), 48 atoms on surface edges (orbit (viii)) and 12 atoms on surface vertexes (orbit (ix)). By distributing different numbers of Ni (or Co) atoms, replacing Pt atoms, in this cuboctahedral structural framework, after geometry relaxation we obtain clusters with varying compositions and compositional orders (Supplementary Fig. 13) that model the stoichiometry and structural features of the different systems produced experimentally. The Cartesian coordinates of these models are reported at the end of the Supplementary Data file. We thus considered one pure Pt model, Pt_{147}, and two $Pt_{122}Ni_{25}$, one $Pt_{131}Ni_{16}$, one $Pt_{134}Ni_{13}$, one $Pt_{116}Ni_{31}$ and one $Pt_{122}Ni_{17}Co_8$ models. In detail, in the mixed sd-$Pt_{122}Ni_{25}$, the 25 Ni atoms were distributed in orbits (i) and (iv), therefore maximizing the number of Pt–Ni bonds. In the segregated fd-$Pt_{122}Ni_{25}$, the same number of 25 Ni atoms were distributed in orbits (i), (ii) and (v). The sd-$Pt_{122}Ni_{25}$ thus mimics an ordered arrangement of Ni in the cluster, as obtained via a slow leaching together with atomic reordering of Ni into an energetically stable distribution, whereas fd-$Pt_{122}Ni_{25}$ mimics a more aggregated arrangement of Ni atoms in the structural framework, as obtained via a fast leaching of the most peripheral Ni atoms.

By electrochemical ADT, further Ni is leached out of the clusters, which we model using two more clusters: (1) in the mixed sd-$Pt_{131}Ni_{16}$-ADT, we started from sd-$Pt_{122}Ni_{25}$, depleted orbit (i) of Ni and replaced one Ni atom with one Pt from each (111) subfacet site (that is, orbit (iv)) to obtain a still reasonably symmetric, strongly mixed and stable Ni distribution but a lower Ni content; and (2) in the segregated fd-$Pt_{134}Ni_{13}$-ADT, we started from fd-$Pt_{122}Ni_{25}$ and depleted orbit (v) of Ni to obtain a strongly segregated and dealloyed cluster. Finally, a sd-$Pt_{122}Ni_{17}Co_8$ model was built by replacing one Ni atom of sd-$Pt_{122}Ni_{25}$ with one Co from each subsurface (111) facet of orbit (iv) to obtain a cluster with the same number of dopant atoms as sd-$Pt_{122}Ni_{25}$ and fd-$Pt_{122}Ni_{25}$ for direct comparison with the experimental particles; this cluster mimics a slow-dealloying process of a PtNiCo particle. For completeness, we also considered a $L1_0$-$Pt_{116}Ni_{31}$ cluster, in which the Ni atoms are distributed in the core according to a $L1_0$-bulk-like chemical ordering, that is, with Pt and Ni alternating in (100) layers. Note that the stoichiometry of our cluster models tries to resemble the experimental ones, given the constraints due to the smallness of our clusters. The geometry of these cluster models was fully relaxed at the DFT or Perdew–Burke–Ernzerhof level, and then used to simulate XANES spectra with the FEFF9 code.

Finally, we calculated oxygen adsorption energies on various sites of the so-derived cluster models (Supplementary Figs. 16 and 19) after full geometry relaxation as $\Delta E_O = E(M_{147}\text{–}O) - E(M_{147}) - E(O_{gas\text{-}phase})$, where all energies are taken at the corresponding equilibrium geometries. We considered the interaction of O adatoms both on the face-centered cubic (111) adsorption sites (as models of the ORR mechanism, to be related to ORR activity) and on vertex sites (as models of particle oxidation/degradation, to be related to the stability of the clusters[48]). In the case of multiple possible adsorption sites inequivalent by symmetry, we took the average adsorption energy to build the plots in the main text and Supplementary Fig. 16.

In detail, the O binding energy, ΔE_O, is calculated as

$$\Delta E_O = E(M_{147}\text{–}O) - E(M_{147}) - E(O_{gas-phase}), \quad (1)$$

where M_{147} is the 147-atom Pt or Pt-alloy cluster model, $E(M_{147}\text{–}O)$ is the total energy of a cluster with O binding on a 147-atom Pt or Pt-alloy cluster, $E(M_{147})$ is the total energy of the 147-atom Pt or Pt-alloy cluster without adsorbates and $E(O_{gas\text{-}phase})$ is the total energy of an oxygen atom in the gas phase.

In the main text, $\Delta E^{(111)}{}_O$ represents the average ΔE_O on the (111) sites of the 147-atom Pt-alloy cluster, $\Delta E^{Pt(111)}{}_O$ represents the average ΔE_O on the (111) sites of the Pt_{147} cluster, $\Delta E^{(Vertex)}{}_O$ represents the ΔE_O on the vertex site of the 147-atom Pt-alloy cluster and $\Delta E^{Pt(Vertex)}{}_O$ represents the ΔE_O on the vertex site of the Pt_{147} cluster.

Note that, in analogy with previous literature[48], we used the oxygen adsorption on the vertex site and the mixing energy (that is, the formation energy; Supplementary Fig. 19) of the clusters as descriptors of their stability (that is, their smaller tendency to Pt oxide formation). Although the topic of aqueous dissolution is important and the focus of current active research, and more advanced approaches have recently been proposed[62], our assumption is reasonable considering, for example, that experimentally, a surface metal oxide on edges and vertexes of Pt nanoparticles has been proven to increase the catalyst stability by protecting undercoordinated and more strongly oxygen-interacting Pt sites such as vertex ones[47].

Note that we use an isolated oxygen atom in the gas phase as a reference. Another reference state for reporting oxygen adsorption, commonly used in previous literature, is the O_2 molecule in the gas phase. To convert the two, it is sufficient to add a positive term of $\frac{1}{2}E(O_{2,gas\text{-}phase}) - E(O_{gas\text{-}phase}) = 2.8$ eV to our O adsorption number.

The mixing energy[46] of an A–B alloy is defined as

$$\Delta[N_A, N_B] = E_{alloy}[N_A, N_B] - N_A E_A[N]/N - N_B E_B[N]/N \quad (2)$$

where $E_{alloy}[N_A, N_B]$ is the energy of a nanoalloy cluster composed of N_A atoms of species A and N_B atoms of species B; $N = N_A + N_B$ is the total number of atoms in the cluster; $E_A[N]$ is the energy of a pure-A cluster of N atoms; and $E_B[N]$ is the energy of a pure-B cluster of N atoms.

Data availability

The atomic coordinates of the DFT calculation data and simulated XANES data are available in the Supplementary Data. The data that support the findings of this study are available from the corresponding authors upon reasonable request. Source data are provided with this paper.

Received: 12 July 2021; Accepted: 26 April 2022;

References

1. Wu, J. & Yang, H. Platinum-based oxygen reduction electrocatalysts. *Acc. Chem. Res.* **46**, 1848–1857 (2013).
2. Nørskov, J. K. et al. Origin of the overpotential for oxygen reduction at a fuel-cell cathode. *J. Phys. Chem. B* **108**, 17886–17892 (2004).
3. Peng, Z. & Yang, H. Designer platinum nanoparticles: control of shape, composition in alloy, nanostructure and electrocatalytic property. *Nano Today* **4**, 143–164 (2009).
4. Debe, M. K. Electrocatalyst approaches and challenges for automotive fuel cells. *Nature* **486**, 43–51 (2012).
5. Kodama, K., Nagai, T., Kuwaki, A., Jinnouchi, R. & Morimoto, Y. Challenges in applying highly active Pt-based nanostructured catalysts for oxygen reduction reactions to fuel cell vehicles. *Nat. Nanotechnol.* **16**, 140–147 (2021).
6. Greeley, J. et al. Alloys of platinum and early transition metals as oxygen reduction electrocatalysts. *Nat. Chem.* **1**, 552–556 (2009).
7. Rossmeisl, J., Karlberg, G. S., Jaramillo, T. & Nørskov, J. K. Steady state oxygen reduction and cyclic voltammetry. *Faraday Discuss.* **140**, 337–346 (2009).
8. Zhang, L. et al. Platinum-based nanocages with subnanometer-thick walls and well-defined, controllable facets. *Science* **349**, 412–416 (2015).
9. Kitchin, J. R., Nørskov, J. K., Barteau, M. A. & Chen, J. G. Modification of the surface electronic and chemical properties of Pt(111) by subsurface 3d transition metals. *J. Chem. Phys.* **120**, 10240–10246 (2004).
10. Zhao, Z. et al. Pt-based nanocrystal for electrocatalytic oxygen reduction. *Adv. Mater.* **31**, 1808115 (2019).
11. Toda, T., Igarashi, H., Uchida, H. & Watanabe, M. Enhancement of the electroreduction of oxygen on Pt alloys with Fe, Ni, and Co. *J. Electrochem. Soc.* **146**, 3750–3756 (1999).
12. Stamenkovic, V. R. et al. Trends in electrocatalysis on extended and nanoscale Pt-bimetallic alloy surfaces. *Nat. Mater.* **6**, 241–247 (2007).
13. Stephens, I. E. L. et al. Tuning the activity of Pt(111) for oxygen electroreduction by subsurface alloying. *J. Am. Chem. Soc.* **133**, 5485–5491 (2011).
14. Escudero-Escribano, M. et al. Tuning the activity of Pt alloy electrocatalysts by means of the lanthanide contraction. *Science* **352**, 73–76 (2016).
15. Strasser, P. et al. Lattice-strain control of the activity in dealloyed core–shell fuel cell catalysts. *Nat. Chem.* **2**, 454–460 (2010).
16. Kitchin, J. R., Nørskov, J. K., Barteau, M. A. & Chen, J. G. Role of strain and ligand effects in the modification of the electronic and chemical properties of bimetallic surfaces. *Phys. Rev. Lett.* **93**, 156801 (2004).
17. Liu, Z., Zhao, Z., Peng, B., Duan, X. & Huang, Y. Beyond extended surfaces: understanding the oxygen reduction reaction on nanocatalysts. *J. Am. Chem. Soc.* **142**, 17812–17827 (2020).
18. Chen, Y., Cheng, T. & Goddard, W. A. III Atomistic explanation of the dramatically improved oxygen reduction reaction of jagged platinum nanowires, 50 times better than Pt. *J. Am. Chem. Soc.* **142**, 8625–8632 (2020).
19. Bligaard, T. & Nørskov, J. K. Ligand effects in heterogeneous catalysis and electrochemistry. *Electrochim. Acta* **52**, 5512–5516 (2007).
20. Calle-Vallejo, F. et al. Finding optimal surface sites on heterogeneous catalysts by counting nearest neighbors. *Science* **350**, 185–189 (2015).
21. Cui, C., Gan, L., Heggen, M., Rudi, S. & Strasser, P. Compositional segregation in shaped Pt alloy nanoparticles and their structural behaviour during electrocatalysis. *Nat. Mater.* **12**, 765–771 (2013).
22. Cherevko, S., Kulyk, N. & Mayrhofer, K. J. J. Durability of platinum-based fuel cell electrocatalysts: dissolution of bulk and nanoscale platinum. *Nano Energy* **29**, 275–298 (2016).
23. Calle-Vallejo, F. et al. Why conclusions from platinum model surfaces do not necessarily lead to enhanced nanoparticle catalysts for the oxygen reduction reaction. *Chem. Sci.* **8**, 2283–2289 (2017).
24. Chattot, R. et al. Surface distortion as a unifying concept and descriptor in oxygen reduction reaction electrocatalysis. *Nat. Mater.* **17**, 827–833 (2018).
25. Bu, L. et al. Biaxially strained PtPb/Pt core/shell nanoplate boosts oxygen reduction catalysis. *Science* **354**, 1410–1414 (2016).
26. Tian, X. et al. Engineering bunched Pt-Ni alloy nanocages for efficient oxygen reduction in practical fuel cells. *Science* **366**, 850–856 (2019).
27. Li, M. et al. Ultrafine jagged platinum nanowires enable ultrahigh mass activity for the oxygen reduction reaction. *Science* **354**, 1414–1419 (2016).
28. Zhang, C., Hwang, S. Y. & Peng, Z. Size-dependent oxygen reduction property of octahedral Pt–Ni nanoparticle electrocatalysts. *J. Mater. Chem. A* **2**, 19778–19787 (2014).
29. Wang, C. et al. Correlation between surface chemistry and electrocatalytic properties of monodisperse Pt_xNi_{1-x} nanoparticles. *Adv. Funct. Mater.* **21**, 147–152 (2011).
30. Huang, X. et al. A rational design of carbon-supported dispersive Pt-based octahedra as efficient oxygen reduction reaction catalysts. *Energy Environ. Sci.* **7**, 2957–2962 (2014).
31. Fortunelli, A. et al. The atomistic origin of the extraordinary oxygen reduction activity of Pt_3Ni_7 fuel cell catalysts. *Chem. Sci.* **6**, 3915–3925 (2015).
32. Gong, M. et al. Optimizing PtFe intermetallics for oxygen reduction reaction: from DFT screening to *in situ* XAFS characterization. *Nanoscale* **11**, 20301–20306 (2019).
33. Wang, T. et al. Sub-6 nm fully ordered $L1_0$-Pt–Ni–Co nanoparticles enhance oxygen reduction via Co doping induced ferromagnetism enhancement and optimized surface strain. *Adv. Energy Mater.* **9**, 1803771 (2019).
34. Dutta, I. et al. Electrochemical and structural study of a chemically dealloyed PtCu oxygen reduction catalyst. *J. Phys. Chem. C* **114**, 16309–16320 (2010).
35. Hwang, B. J. et al. An investigation of structure−catalytic activity relationship for Pt−Co/C bimetallic nanoparticles toward the oxygenreduction reaction. *J. Phys. Chem. C* **111**, 15267–15276 (2007).
36. Moraweck, B., Renouprez, A. J., Hlil, E. K. & Baudoing-Savois, R. Alloying effects on X-ray absorption edges in nickel-platinum single crystals. *J. Phys. Chem.* **97**, 4288–4292 (1993).
37. Hlil, E. K., BaudoingSavois, R., Moraweck, B. & Renouprez, A. J. X-ray absorption edges in platinum-based alloys. 2. Influence of ordering and of the nature of the second metal. *J. Phys. Chem.* **100**, 3102–3107 (1996).
38. Chen, J. et al. Elucidating the many-body effect and anomalous Pt and Ni core level shifts in X-ray photoelectron spectroscopy of Pt–Ni alloys. *J. Phys. Chem. C* **124**, 2313–2318 (2020).
39. Mukerjee, S., Srinivasan, S., Soriaga, M. P. & Mcbreen, J. Role of structural and electronic-properties of Pt and Pt alloys on electrocatalysis of oxygen reduction: an *in-situ* XANES and EXAFS investigation. *J. Electrochem. Soc.* **142**, 1409–1422 (1995).
40. Rehr, J. J., Kas, J. J., Vila, F. D., Prange, M. P. & Jorissen, K. Parameter-free calculations of X-ray spectra with FEFF9. *Phys. Chem. Chem. Phys.* **12**, 5503–5513 (2010).
41. Pápai, Z. & Pap, T. L. Analysis of peak asymmetry in chromatography. *J. Chromatogr. A* **953**, 31–38 (2002).
42. Kuhn, M. & Sham, T. K. Charge redistribution and electronic behavior in a series of Au-Cu alloys. *Phys. Rev. B* **49**, 1647–1661 (1994).
43. Jia, Q. et al. Activity descriptor identification for oxygen reduction on platinum-based bimetallic nanoparticles: *in situ* observation of the linear composition–strain–activity relationship. *ACS Nano* **9**, 387–400 (2015).
44. Cao, L. et al. Differential surface elemental distribution leads to significantly enhanced stability of PtNi-based ORR catalysts. *Matter* **1**, 1567–1580 (2019).
45. Li, J. et al. Hard-magnet $L1_0$-CoPt nanoparticles advance fuel cell catalysis. *Joule* **3**, 124–135 (2019).
46. Barcaro, G., Sementa, L. & Fortunelli, A. A grouping approach to homotop global optimization in alloy nanoparticles. *Phys. Chem. Chem. Phys.* **16**, 24256–24265 (2014).
47. Hu, J. et al. Increasing stability and activity of core–shell catalysts by preferential segregation of oxide on edges and vertexes: oxygen reduction on Ti–Au@Pt/C. *J. Am. Chem. Soc.* **138**, 9294–9300 (2016).
48. Jennings, P. C., Aleksandrov, H. A., Neyman, K. M. & Johnston, R. L. A DFT study of oxygen dissociation on platinum based nanoparticles. *Nanoscale* **6**, 1153–1165 (2014).
49. Arán-Ais, R. M. et al. Elemental anisotropic growth and atomic-scale structure of shape-controlled octahedral Pt–Ni–Co alloy nanocatalysts. *Nano Lett.* **15**, 7473–7480 (2015).
50. Zhao, Z. et al. Composition tunable ternary Pt–Ni–Co octahedra for optimized oxygen reduction activity. *ChemComm* **52**, 11215–11218 (2016).
51. Huang, X. et al. High-performance transition metal–doped Pt_3Ni octahedra for oxygen reduction reaction. *Science* **348**, 1230–1234 (2015).
52. Huang, J. et al. PtCuNi tetrahedra catalysts with tailored surfaces for efficient alcohol oxidation. *Nano Lett.* **19**, 5431–5436 (2019).
53. Arruda, T. M., Shyam, B., Ziegelbauer, J. M., Mukerjee, S. & Ramaker, D. E. Investigation into the competitive and site-specific nature of anion adsorption on Pt using in situ X-ray absorption spectroscopy. *J. Phys. Chem. C* **112**, 18087–18097 (2008).
54. Newville, M. IFEFFIT: interactive XAFS analysis and FEFF fitting. *J. Synchrotron Radiat.* **8**, 322–324 (2001).
55. Ravel, B. & Newville, M. ATHENA, ARTEMIS, HEPHAESTUS: data analysis for X-ray absorption spectroscopy using IFEFFIT. *J. Synchrotron Radiat.* **12**, 537–541 (2005).
56. Newville, M., Līviņš, P., Yacoby, Y., Rehr, J. J. & Stern, E. A. Near-edge X-ray-absorption fine structure of Pb: a comparison of theory and experiment. *Phys. Rev. B* **47**, 14126–14131 (1993).
57. Ankudinov, A. L., Ravel, B., Rehr, J. J. & Conradson, S. D. Real-space multiple-scattering calculation and interpretation of X-ray-absorption near-edge structure. *Phys. Rev. B* **58**, 7565–7576 (1998).
58. Mattheiss, L. F. Energy bands for solid argon. *Phys. Rev.* **133**, A1399–A1403 (1964).
59. Giannozzi, P. et al. QUANTUM ESPRESSO: a modular and open-source software project for quantum simulations of materials. *J. Condens. Matter Phys.* **21**, 395502 (2009).
60. Perdew, J. P., Burke, K. & Ernzerhof, M. Generalized gradient approximation made simple. *Phys. Rev. Lett.* **77**, 3865–3868 (1996).

61. Vanderbilt, D. Soft self-consistent pseudopotentials in a generalized eigenvalue formalism. *Phys. Rev. B* **41**, 7892–7895 (1990).
62. Wang, Z., Guo, X., Montoya, J. & Nørskov, J. K. Predicting aqueous stability of solid with computed Pourbaix diagram using SCAN functional. *npj Comput. Mater.* **6**, 160 (2020).
63. Chen, C. et al. Highly crystalline multimetallic nanoframes with three-dimensional electrocatalytic surfaces. *Science* **343**, 1339–1343 (2014).
64. Gong, M. et al. One-nanometer-thick Pt_3Ni bimetallic alloy nanowires advanced oxygen reduction reaction: integrating multiple advantages into one catalyst. *ACS Catal.* **9**, 4488–4494 (2019).
65. Beermann, V. et al. Rh-doped Pt–Ni octahedral nanoparticles: understanding the correlation between elemental distribution, oxygen reduction reaction, and shape stability. *Nano Lett.* **16**, 1719–1725 (2016).
66. Lim, J. et al. Ga–doped Pt–Ni octahedral nanoparticles as a highly active and durable electrocatalyst for oxygen reduction reaction. *Nano Lett.* **18**, 2450–2458 (2018).
67. Bu, L. et al. Surface engineering of hierarchical platinum-cobalt nanowires for efficient electrocatalysis. *Nat. Commun.* **7**, 11850 (2016).

Acknowledgements

Y.H., Q.J., W.A.G. and X.D. gratefully acknowledge the support of the Office of Naval Research (award N000141812155). The XAS data were collected at beamlines 6-BM, 7-BM and 8-ID of the National Synchrotron Light Source II, a US Department of Energy Office of Science User Facility operated for the Department of Energy Office of Science by Brookhaven National Laboratory under contract no. DE-SC0012704. We acknowledge the use of facilities and instrumentation at the University of California Irvine Materials Research Institute, supported in part by the National Science Foundation Materials Research Science and Engineering Center programme through the University of California Irvine Center for Complex and Active Materials (DMR-2011967). We also thank the Electron Imaging Center of Nanomachines at CNSI for TEM support. A.F. and W.A.G. received support from the National Science Foundation (CBET-1805022 and CBET-2005250). A.F., G.B. and L.S. gratefully acknowledge the contribution of the International Research Network on Nanoalloys (CNRS) and computational support from the CINECA supercomputing centre within the ISCRA programme.

Author contributions

J.H., M.F., M.L., Y.L., C.W., S.-J.L., B.P. and Z.L. conducted the synthesis of electrocatalysts, structural characterization and electrochemical experiments. M.X. and J.H. conducted the TEM and EDX characterizations. Q.J., E.L., J.L. and D.L. conducted the XAS studies. A.F., L.S., G.B., Q.J., J.H. and W.A.G. performed the modelling and data analyses. The project was supervised by Y.H. (conceptualization, project design, syntheses and evaluation of the catalysts); Q.J. (XAS studies); and A.F. and W.A.G. (computational studies). J.H., Y.H., Q.J. and A.F. wrote the original draught. J.H., Y.H., Q.J., A.F., W.A.G. and Z.L. helped revise the paper.

Competing interests

The authors declare no competing interests.

Additional information

Supplementary information The online version contains supplementary material available at https://doi.org/10.1038/s41929-022-00797-0.

Correspondence and requests for materials should be addressed to William A. Goddard, Alessandro Fortunelli, Qingying Jia or Yu Huang.

Peer review information *Nature Catalysis* thanks Janis Timoshenko and the other, anonymous, reviewer(s) for their contribution to the peer review of this work.

Reprints and permissions information is available at www.nature.com/reprints.

Publisher's note Springer Nature remains neutral with regard to jurisdictional claims in published maps and institutional affiliations.

QUERY FORM

Nature Catalysis	
Manuscript ID	**[Art. Id: 797]**
Author	**Jin Huang**

AUTHOR:

The following queries have arisen during the editing of your manuscript. Please answer by making the requisite corrections directly in the e.proofing tool rather than marking them up on the PDF. This will ensure that your corrections are incorporated accurately and that your paper is published as quickly as possible.

Query No.	*Nature of Query*
Q1:	Your paper has been copy edited. Please review every sentence to ensure that it conveys your intended meaning; if changes are required, please provide further clarification rather than reverting to the original text. Please note that formatting (including hyphenation, Latin words, and any reference citations that might be mistaken for exponents) has been made consistent with our house style.
Q2:	Please note, we reserve 'significant' and its derivatives for statistical significance. Please reword where this is not the intended meaning (for example to important, notable, substantial); there are 5 instances throughout your text.
Q3:	Please check your article carefully, coordinate with any co-authors and enter all final edits clearly in the eproof, remembering to save frequently. Once corrections are submitted, we cannot routinely make further changes to the article.
Q4:	Note that the eproof should be amended in only one browser window at any one time; otherwise changes will be overwritten.
Q5:	Author surnames have been highlighted. Please check these carefully and adjust if the first name or surname is marked up incorrectly. Note that changes here will affect indexing of your article in public repositories such as PubMed. Also, carefully check the spelling and numbering of all author names and affiliations, and the corresponding email address(es).
Q6:	You cannot alter accepted Supplementary Information files except for critical changes to scientific content. If you do resupply any files, please also provide a brief (but complete) list of changes. If these are not considered scientific changes, any altered Supplementary files will not be used, only the originally accepted version will be published.
Q7:	If applicable, please ensure that any accession codes and datasets whose DOIs or other identifiers are mentioned in the paper are scheduled for public release as soon as possible, we recommend within a few days of submitting your proof, and update the database record with publication details from this article once available.
Q8:	In the sentence beginning 'Herein, by combining...' please clarify the meaning of 'strain' in 'EXAFS; strain'.
Q9:	In the sentence beginning 'We hence chose...' please confirm the edit of the unit '$\%_{atom}$' to 'at.%', or clarify the meaning.
Q10:	Please confirm that edits to the sentence beginning 'We designed and...' have retained the intended meaning. The definition of DMF was edited to match the definition given later in the paper.

QUERY FORM

Nature Catalysis	
Manuscript ID	**[Art. Id: 797]**
Author	**Jin Huang**

AUTHOR:

The following queries have arisen during the editing of your manuscript. Please answer by making the requisite corrections directly in the e.proofing tool rather than marking them up on the PDF. This will ensure that your corrections are incorporated accurately and that your paper is published as quickly as possible.

Query No.	*Nature of Query*
Q11:	Please confirm all edits in the graphical abstract.
Q12:	(1) Please confirm all edits in Fig. 1 and its caption.
Q13:	In the sentence beginning 'It was found that the composition...' please clarify the meaning of '-ADT' added to the species.
Q14:	In the sentence beginning 'Indeed, the linear...' please clarify the difference between SA and SA_Pt and confirm all edits.
Q15:	In the sentence beginning 'Indeed, the linear...', please define R^2.
Q16:	In the sentence beginning ' In particular, the Pt...' please clarify the meaning of 'its'; does this mean the density of states?
Q17:	(1) Please confirm all edits in Fig. 2 and its caption. (2) Please define μ or χμ(E). (3) In 2b, please clarify, similar to what?
Q18:	In the sentence beginning 'Notably, the ΔAF..' please clarify the meaning of 'its' in 'its impact'.
Q19:	In the sentence beginning 'In addition, an...' please clarify the meaning of '$L1_0$' in '$L1_0$-$Pt_{116}Ni_{31}$'.
Q20:	In the sentence beginning 'Importantly, the broadening...' please clarify the meaning of the ending. Do you mean 'to obtain experimentally and to apply in catalyst performance prediction' for example?
Q21:	(1) Please confirm all edits in Fig. 3 and its caption. (2) In 3d, please confirm the edit to the meaning of the asterisk. (3) In 3d, please clarify the use of plural 'error bars' when only one error bar is seen. (4) In 3b and 3e, please define R (with no subscript as in the Methods) and j.
Q22:	Please note: the prefix oct was edited to lowercase to be consistent with the prefix tetra.
Q23:	(1) Please confirm all edits in Fig. 4 and its caption. (2) What do the shaded areas and the horizontal dashed line represent in 4b? (3) In 4c, please define abbreviations in the literature species (like NW) if needed. (4) In 4c, please describe in the caption what the non-hollow circles show.
Q24:	In the section 'Chemicals', please confirm the insertion of 'parts per 10^{12}' as the definition of 'ppt' is correct.
Q25:	In the sentence beginning 'The ECSA was...' please confirm that H_upd is a variable.
Q26:	In the sentence beginning 'The current density...', please define iR.

QUERY FORM

Nature Catalysis	
Manuscript ID	**[Art. Id: 797]**
Author	**Jin Huang**

AUTHOR:

The following queries have arisen during the editing of your manuscript. Please answer by making the requisite corrections directly in the e.proofing tool rather than marking them up on the PDF. This will ensure that your corrections are incorporated accurately and that your paper is published as quickly as possible.

Query No.	*Nature of Query*
Q27:	In the sentence beginning 'The mass activity...', please define $V_{iR\text{-}free}$ and kPa_{abs}, and confirm that RH meant relative humidity.
Q28:	In the sentence beginning 'The H2/air test...', please define stoi.
Q29:	In the sentence beginning 'The χ(R) were...', please define χ(R).
Q30:	In the sentence beginning 'Here RPt–Ni...', please define D-E factor.
Q31:	Please confirm that edits to the sentence beginning 'By distributing different ...' have retained the intended meaning. Or, did you mean 'By distributing different numbers of Ni (or Co) atoms by different methods'?
Q32:	Please confirm that edits to the sentence beginning 'The geometry of ...' have retained the intended meaning. Or, did you mean 'DFT and Perdew–Burke–Ernzerhof levels'?
Q33:	In eq. 1 and the surrounding text, should the species in () like M_147 and O_gas-phase be subscript to E, for consistency?
Q34:	Please confirm the double negatives in eq. 1.
Q35:	In the journal's style, square brackets are used to mean concentration. Please confirm that the use [] is needed in equation 2, or edit to ().
Q36:	The Author contributions have been edited for style. Please confirm.
Q37:	In the Author contributions, please clarify which author J.L. is; should this be J.H. or L.J.?
Q38:	In the Acknowledgements, please define CNSI, CNRS and ISCRA.